Showcasing research from Professor Flavio Maran's and Professor Marco Ruzzi's laboratories, Department of Chemistry, University of Padova, Italy.

Understanding and controlling the efficiency of $Au_{24}M(SR)_{18}$ nanoclusters as singlet-oxygen photosensitizers

Singlet oxygen, $^1O_2$, is a reactive oxygen species that can be generated by photisensitizers for important applications. We photoexcited atomically precise $Au_{24}M(SR)_{18}$ clusters, carrying different R groups and doping metal atoms M, and could efficiently detect the transient formation of $^1O_2$ by time-resolved electron paramagnetic resonance. We found that a more difficult oxidation of the molecular cluster corresponds to a longer $^1O_2$ lifetime. Kinetic analysis led to important insights into controlling the performance of gold nanoclusters as compelling $^1O_2$ photosensitizers.

As featured in:

Chemical Science

ROYAL SOCIETY OF CHEMISTRY

rsc.li/chemical-science

ROYAL SOCIETY OF CHEMISTRY

Check for updates

Understanding and controlling the efficiency of Au₂₄M(SR)₁₈ nanoclusters as singlet-oxygen photosensitizers†

Mikhail Agrachev, ‡[a] Wenwen Fei, ‡[a] Sabrina Antonello, [a] Sara Bonacchi, [a] Tiziano Dainese, [a] Alfonso Zoleo, [a] Marco Ruzzi *[a] and Flavio Maran *[ab]

Singlet oxygen, $^1O_2$, can be generated by molecules that upon photoexcitation enable the $^3O_2 \rightarrow {}^1O_2$ transition. We used a series of atomically precise Au₂₄M(SR)₁₈ clusters, with different R groups and doping metal atoms M. Upon nanosecond photoexcitation of the cluster, $^1O_2$ was efficiently generated. Detection was carried out by time-resolved electron paramagnetic resonance (TREPR) spectroscopy. The resulting TREPR transient yielded the $^1O_2$ lifetime as a function of the nature of the cluster. We found that: these clusters indeed generate $^1O_2$ by forming a triplet state; a more positive oxidation potential of the molecular cluster corresponds to a longer $^1O_2$ lifetime; proper design of the cluster yields results analogous to those of a well-known reference photosensitizer, although more effectively. Comprehensive kinetic analysis provided important insights into the mechanism and driving-force dependence of the quenching of $^1O_2$ by gold nanoclusters. Understanding on a molecular basis why these molecules may perform so well in $^1O_2$ photosensitization is instrumental to controlling their performance.

Introduction

Singlet oxygen, $^1O_2$, is the first excited state ($^1\Delta_g$) of molecular oxygen. Depending on the experimental conditions, its lifetime can span several orders of magnitude.[1–3] $^1O_2$ eventually converts to ground-state triplet oxygen ($^3\Sigma_g^-$), $^3O_2$. Because singlet oxygen is significantly more reactive than triplet oxygen, it finds uses in several applications, especially organic synthesis, photocatalysis, and nanomedicine (photodynamic therapy).[4–9] Singlet oxygen[10–12] can be produced by direct excitation, although $^3O_2 \rightarrow {}^1O_2$ is a spin-forbidden transition with a very low absorption coefficient. A more efficient way to generate singlet oxygen is by using photosensitizers.[10,13] The sensitizer is photoexcited to its singlet state, undergoes intersystem crossing (ISC) to form the excited triplet state, and then transfers energy to triplet oxygen to yield $^1O_2$; the last step is efficient because the overall angular moment is now conserved. Suitable photosensitizers are molecules that exhibit a sufficiently high value of the excited triplet-state energy (the $^3\Sigma_g^-$ to $^1\Delta_g$ excitation energy,

E_{exc}, is 94 kJ mol^{-1}), a high quantum yield for ISC, and a sufficiently long triplet lifetime. On the other hand, it has been long acknowledged that the sensitizer and/or products of its photoreactions can also quench singlet oxygen by converting it back to $^3O_2$.[14,15] These quenching reactions may significantly diminish the $^1O_2$ lifetime and, consequently, affect the overall efficiency of the photosensitization process. An ideal photosensitizer should, therefore, maximize generation efficiency and minimize deactivation. This is not, however, an easy task to achieve.[10]

The detection of singlet oxygen in fluid solution is routinely carried out by optical spectroscopy. The most specific probe of singlet oxygen is 1275 nm $^1O_2 \rightarrow {}^3O_2$ phosphorescence, particularly when it is monitored in a time-resolved experiment. To overcome the low-sensitivity limitations, several approaches have been proposed, mostly relying on the introduction of a fluorescent probe activated by energy transfer from $^1O_2$. For example, phthalocyanines, naphthalocyanines, and porphyrazines exhibit strong delayed luminescence upon energy transfer from two $^1O_2$ molecules.[16] This luminescence is emitted in the visible-light region and its quantum yield exceeds that of $^1O_2$ phosphorescence by 2–4 orders of magnitude. These molecules, however, are also good sensitizers for the formation of $^1O_2$, thereby complicating detection. Chemical traps have also been extensively employed.[17] Singlet oxygen rapidly and irreversibly reacts with aromatic compounds to yield endoperoxides that do not fluoresce and whose absorption spectrum differs significantly from that of the original molecule.

[a]Department of Chemistry, University of Padova, Via Marzolo 1, 35131 Padova, Italy. E-mail: marco.ruzzi@unipd.it; flavio.maran@unipd.it

[b]Department of Chemistry, University of Connecticut, 55 North Eagleville Road, Storrs, 06269 Connecticut, USA

† Electronic supplementary information (ESI) available: Chemicals, determination of relevant kinetic and thermodynamic parameters, further experimental procedures, Table S1 and Fig. S1–S9. See DOI: 10.1039/d0sc00520g

‡ Co-first authors.

However, chemical traps may also be reactive toward other reactive oxygen species. Because of the difficulties associated with direct detection and indirect methods, alternative approaches for the detection of $^1O_2$ generated by photosensitizers are thus sought.

Possible photosensitizer candidates that meet several of the aforementioned requirements are atomically precise gold nanoclusters, $Au_n(SR)_m$ (where SR = thiolate). Nowadays, many of these clusters can be prepared in a very pure, controlled state.[18] This implies full molecular control on the structure and properties, which cannot be achieved with the larger gold nanoparticles. Because the electronic structure and thus the optical properties of these clusters depend on the values of n and m, ultrasmall gold nanoclusters might be, in principle, optimized for the efficient production of $^1O_2$. So far, the research in this field has been quite limited,[19–33] with very few examples describing the behavior of truly atomically precise gold nanoclusters. This is the case of $Au_{25}(SR)_{18}$, which is a stable cluster that shows distinct electrochemical,[34] optical,[18] and magnetic features,[35,36] and is consistently considered the benchmark system for understanding and controlling many properties of gold nanoclusters.[37,38] Kawasaki et al. were the first to describe the formation of singlet oxygen using $Au_{25}(SR)_{18}$ (HSR = phenylethanethiol or captopril) as the photosensitizer.[19] The photosensitization was detected optically and with chemical quenchers. $Au_{38}(SC_2H_4Ph)_{24}{}^0$, another well-established molecular cluster, was found to be significantly less efficient. More recently, Ho-Wu et al. compared the photosensitization efficiency of Au_{25}, Ag_{32}, Au_{144}, larger gold nanoparticles, and a conventional dye photosensitizer.[29] This study, which was carried out with indirect optical methods (1,3-diphenyliso-benzofuran quencher), concluded that Au_{144} provides the most efficient system. A size dependence order of $Au_{144} > Au_{38} > Au_{25}$ was observed for the aerobic oxidation of D-glucose on carbon-supported clusters.[31] The efficiency of $^1O_2$ generation using $Au_{38}S_2(SAdm)_{20}$ (SAdm = adamantanethiolate) nanoclusters was found to be higher than that of $Au_{25}(SC_2H_4Ph)_{18}{}^-$.[32] The ultrasonic activation of $Au_{25}(Captopril)_{18}$ to generate $^1O_2$ was also demonstrated.[33]

Here we describe the photosensitizing behavior of a series of $Au_{25}(SR)_{18}{}^-$, where R = n-C_3H_7 (C3), n-C_4H_9 (C4), and C_2H_4Ph (C2Ph) (hereafter, we will indicate the number of carbon atoms of the alkyl chain simply as Cn), and mono-doped $Au_{24}M(SR)_{18}{}^0$ (M = Cd, Hg) clusters (Fig. 1). Besides studying the effect of the protecting ligand, the analysis was extended to monodoped clusters because their optical and especially electrochemical behaviors show significant differences from those of the undoped clusters.[39] Regarding detection, we relied on continuous-wave and, especially, time-resolved electron paramagnetic resonance techniques (CWEPR and TREPR, respectively). TREPR spectroscopy provides an efficient and sensitive method to detect even very low concentrations of $^1O_2$ generated by photosensitization in solution.[40,41] Moreover, TREPR is selective toward singlet oxygen, which is unequivocally detected and identified, while other reactive oxygen species are not revealed. As we will show, TREPR allowed us to characterize in detail the
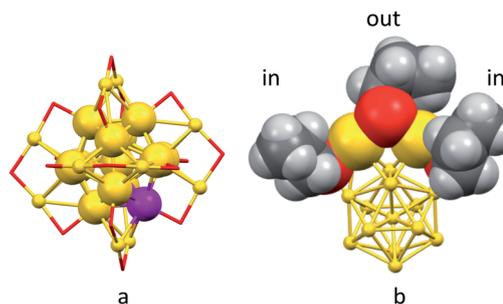

Fig. 1 (a) Typical structure of the $Au_{24}M(SR)_{18}$ nanocluster. One of the icosahedron positions (purple) corresponds to M (M = Au, Hg, Cd). The gold (yellow) and sulfur (red) atoms are shown, whereas the carbonaceous part of the ligands is omitted for clarity. (b) Structure of $Au_{25}(SC3)_{18}{}^0$ showing the C (gray) and H atoms (white) for both inner (in) and outer (out) ligand types of one of the six staples.

photosensitization behavior of the investigated clusters, and could confirm that the cluster's excited state responsible for the generation of singlet oxygen is indeed a triplet. Most notably, we found that proper design of the redox properties of the cluster yields results comparable to those of tetraphenylporphirin (TPP), which is a well-known reference photosensitizer.[10] Finally, we carried out a comprehensive kinetic investigation on the $^1O_2$ quenching mechanism by gold nanoclusters as a function of driving force and obtained important mechanistic insights into the reasons why properly devised gold nanoclusters may perform very well in $^1O_2$ photosensitization.

Results and discussion

### $^1O_2$ photosensitization with TREPR detection

TREPR spectroscopy is especially suitable to study the kinetics of photogenerated paramagnetic species exhibiting lifetimes ranging from a few to several hundred μs.[42] TREPR detection of $^1O_2$ is based on the radical triplet pair (RTP) mechanism.[43] Triplet quenching by a stable free radical, such as a nitroxide (which is a doublet, ^2R, and generally exhibits three, very similar CWEPR lines due to the hyperfine interaction of the unpaired electron with the N nucleus), induces populations of radical spin sublevels that differ significantly from those at thermal equilibrium. This phenomenon, which is commonly referred to as chemically induced dynamic electron polarization,[44] can be sensitively detected by TREPR in the form of transient intensities of the EPR signals associated with the radical probe. Importantly, polarization may also be caused by a singlet state, as in the case of $^1O_2$.[45,46]

Briefly, photoexcitation of the sensitizer fundamental singlet state (^1PS) yields a singlet excited state ($^1PS^*$) that is quickly converted into a triplet state ($^3PS^*$) via ISC. In the absence of oxygen, the excited triplet state undergoes quenching by interaction with a nitroxide radical, and *polarized emissive* TREPR signals are observed. The emissive polarization is interpreted according to quartet-precursor RTP (Q-RTP) theory,[47] as described by eqn (1):

$$^3PS* + {}^2R \rightarrow {}^1PS + {}^2R*\downarrow \qquad (1)$$

where $^2R*\downarrow$ indicates the emissive spin polarization generated in ^2R by the quenching of the $^3PS*$ state. Radicals, on the other hand, are also able to quench singlet states, though now the spin polarization is opposite to that just described: in an air-saturated solution of a nitroxide and a triplet sensitizer, a *reinforced absorptive polarization* for the signals of the nitroxide is indeed expected. This absorptive character of the polarization is a consequence of the initial energy exchange of the triplet state of the sensitizer by triplet oxygen to form $^1O_2$ (eqn (2)), which then polarizes the radical ^2R (eqn (3)):

$$^3PS* + {}^3O_2 \rightarrow {}^1PS + {}^1O_2 \qquad (2)$$

$$^1O_2 + {}^2R \rightarrow {}^3O_2 + {}^2R*\uparrow \qquad (3)$$
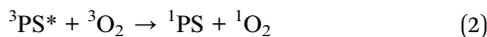
where $^2R*\uparrow$ refers to the radical in which reinforced absorptive spin polarization is generated. This mechanism is the equivalent of the doublet-precursor RTP (D-RTP) theory,[45] the only difference being that now the nitroxide interacts with a singlet, rather than a triplet state. Very importantly, the magnitude of this net absorptive spin polarization is *extraordinarily large* even for traces of singlet oxygen.[46]

All clusters were prepared and characterized by mass spectrometry, NMR spectroscopy, and UV-vis spectroscopy as described previously.[39,48–50] Special attention was paid to controlling properly the charge state.[51,52] TREPR experiments were carried out in toluene at 240 K, and refer to 1 mM clusters and 0.5 mM 2,2,6,6-tetramethyl-4-oxo-1-piperidinyloxy (TEMPONE), unless otherwise stated. In TREPR, a laser pulse (we used 4 ns at 532 nm) triggers the aforementioned photochemical reaction/s and eventually generates the polarized paramagnetic species ($^2R*\uparrow$ or $^2R*\downarrow$). The ensuing EPR transient is recorded at a given value of the magnetic field (B). This procedure is applied by scanning B until the entire field range is covered. The sequence is then repeated many times, and the corresponding series of transients are averaged. The resulting TREPR spectrum is usually displayed in a 3D form (Fig. 2), where the TREPR intensity is plotted as a function of B and time (t). No field modulation is applied and thus the observed signals do not exhibit the derivative shape typical of the corresponding CWEPR spectra (Fig. 3c and d).

Fig. 2a shows the spectrum obtained using $Au_{25}(SC3)_{18}{}^-$ as the photosensitizer under aerobic conditions. The TREPR spectrum of TEMPONE consists of three signals of equal intensity that decay in a few μs. The polarized TREPR signals show the net absorptive character expected when the overall photosensitization process (excitation, ISC, and energy transfer) is efficient and followed by step (3). In the control experiment carried out in the absence of oxygen, only emissive polarization is observed (Fig. 2b). According to the Q-RTP mechanism, the emissive polarized transient spectra are consistent with the direct interaction of the nitroxide with the triplet state of $Au_{25}(SR)_{18}{}^-$. The extent of emissive polarization strongly depends on the quantum yield of the latter and the actual lifetime of the cluster triplet state. In this connection, the
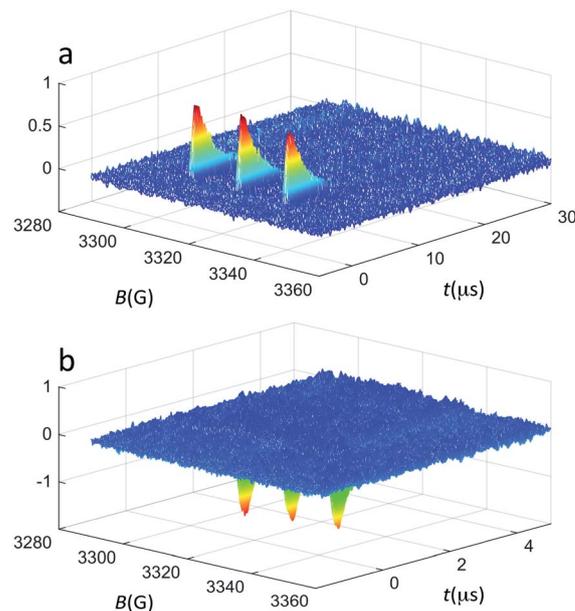

Fig. 2 TREPR surfaces recorded for 0.5 mM TEMPONE and 1 mM $Au_{25}(SC3)_{18}{}^-$ in (a) air-saturated and (b) deaerated toluene solution at 240 K. The z-axis shows the TREPR intensity (a.u.).

different time scales of the transients in the two plots of Fig. 2 are worth noticing. These results already allow us to draw a very important conclusion. So far, photoexcitation of clusters has been generically described as generating excited states, as no conclusive evidence about the formation of an excited triplet state could be gathered. In the first report on singlet oxygen generation by photoexcited Au clusters, the term triplet state was used for the very same reason that the photoexcited cluster was generating $^1O_2$.[19] On the other hand, singlet oxygen may form in several different ways.[53] In the present context, the TREPR results observed under anaerobic conditions definitely
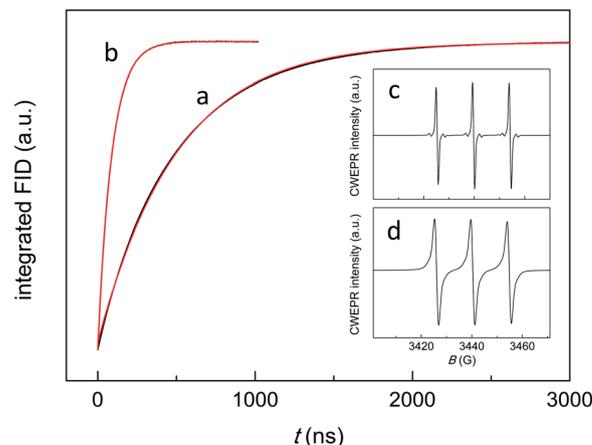

Fig. 3 Inversion recovery curves for a toluene solution of 0.5 mM TEMPONE and 1 mM $Au_{25}(SC3)_{18}{}^-$ (black) under anaerobic (trace (a)) and aerobic conditions (trace (b)), with the corresponding exponential fits to the data (red: for both curves, $r^2 = 1.000$). The CWEPR spectra refer to the corresponding anaerobic (c) and aerobic conditions (d).

prove that, indeed, photoexcitation of $Au_{25}(SR)_{18}{}^-$ eventually leads to an excited triplet state.[46]

Analysis of the $^1O_2$ lifetime and validation of the TREPR method

The decay kinetics depends on several parameters. In a deaerated solution, the decay of the emission-polarized signals (Fig. 2b) is determined by the lifetime of the cluster triplet state and the characteristic magnetic-relaxation times of the nitroxide, T_1 and T_2.[54] T_1, which is the spin-lattice longitudinal relaxation time, can be determined independently, by pulsed EPR inversion recovery experiments (Fig. 3, trace (a)), to be 499.1(0.6) ns. In the absence of the cluster, we obtained a virtually identical value of 501.8(0.7) ns ($r^2 = 1.000$). T_2 is the transverse spin–spin relaxation time and could be estimated to be 0.43(0.01) µs from the reciprocal of the full-width-at-half-height of the integral of the CWEPR spectrum shown in Fig. 3c, as illustrated in Fig. S1.† In deaerated solution, the reciprocal of the TREPR decay rate-constant value obtained from the emission data (Fig. S2†) is 0.45(0.01) µs ($r^2 = 0.983$), and therefore, is comparable to the relaxation parameters of TEMPONE. These results point to the TEMPONE spin relaxation as a particularly relevant factor determining the TREPR decay kinetics and thus imply that the lifetime of the cluster triplet state should be shorter than ~0.3 µs.

In the presence of air, the CWEPR spectrum of TEMPONE shows broader peaks (Fig. 3d). The T_1 measured by pulsed EPR inversion recovery experiments in the presence of $Au_{25}(SC3)_{18}{}^-$ (Fig. 3b) is now only 64(0.2) ns ($r^2 = 1.000$), that is, about one order of magnitude shorter than the T_1 determined under anaerobic conditions. Similarly, T_2 decreases from 0.43 to 0.04 µs. These effects are caused by the known interaction of TEMPONE with triplet oxygen.[55] Under aerobic conditions, the decay of the TREPR signals also depends on the singlet-oxygen

lifetime. A scheme of the general process is provided in the inset of Fig. 4. The average of the TREPR transients (Fig. 4) can be fit to a single exponential ($r^2 = 0.969$) yielding an observed decay rate constant (k_Δ) of 3.02×10^5 s^{-1}, which corresponds to a lifetime (τ_Δ) of 3.31(0.05) µs. τ_Δ is thus nearly two orders of magnitude longer than the corresponding T_1 value, and this indicates that now the observed decay of spin polarization is only controlled by the $^1O_2$ lifetime. In other words, while the polarized signals decay on the T_1 time scale, there is still some singlet oxygen in solution that continuously contributes to generating further polarization in the TEMPONE molecules. Under these conditions, the decay of the TREPR signal lifetime can thus be used to calculate the singlet-oxygen lifetime.

Under any given experimental conditions, the observed $^1O_2$ lifetime is determined by the species present in solution.[10] In the absence of solutes other than oxygen, on the other hand, the intrinsic $^1O_2$ decay pseudo-first order rate constant (k_Δ^S) only depends on the solvent (S) through two terms (eqn (4)):

$$k_\Delta^S = k_{nr}[S] + k_r[S] \tag{4}$$

where k_{nr} and k_r refer to the nonradiative and radiative components, respectively.[10,56] From available data obtained in toluene as a function of temperature, we calculate the intrinsic lifetime of $^1O_2$ (τ_Δ^S) at 240 K to be 31.7 [57] and 34.6 µs.[56] These lifetimes are significantly longer than the lifetime of 3.31 µs obtained with the TEMPONE/$Au_{25}(SC3)_{18}{}^-$ system, and therefore, show that in our experimental conditions significant quenching of singlet oxygen must take place. Comparison of τ_Δ with τ_Δ^S (hereafter, we will refer to the most recent determination, 34.6 µs)[56] yields a relative τ_Δ decrease of $100(\tau_\Delta^S - \tau_\Delta)/\tau_\Delta^S = 90.4\%$.

Besides the solvent, there are two possible candidates as quenchers: TEMPONE and the cluster itself. To address this issue, we carried out further experiments. The majority of photosensitizers currently employed in photodynamic therapy are cyclic tetrapyrrolic structures, such as porphyrin derivatives.[58] It is thus instructive to compare the polarized signals observed for $Au_{25}(SC3)_{18}{}^-$ with those obtained for tetraphenylporphyrin (TPP), which is a well-known reference photosensitizer, yet showing some quenching of $^1O_2$.[59] TPP was used at the same concentration of the cluster (1 mM) and qualitatively gave the same TREPR spectrum, but for the two differences that the signal intensity at its maximum is ~3 times larger than for $Au_{25}(SC3)_{18}{}^-$ and, particularly important, the decay is much slower (Fig. 5). It should be noted that for $t < 0.5$ µs the presence of a negative spike indicates that a (small) fraction of the TPP molecules in their triplet excited state (for TPP, the fraction of singlet excited state species that undergo radiationless decay to form the triplet excited state is $\Phi_T = 0.71$;[60] in the presence of oxygen, this value is expected to increase slightly)[61] react with TEMPONE according to Q-RTP theory (eqn (1)). The fact that the TREPR intensity maximum is attained at 1.5–2 µs indicates that the majority of the TPP triplet reacts with $^3O_2$ within less than 1 µs. This is in keeping with a lifetime of 196 ns measured for the TPP triplet state in aerated toluene at room temperature.[62]
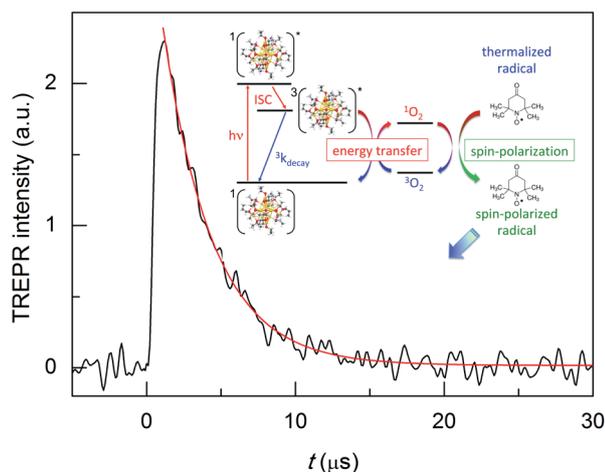

Fig. 4 TREPR transient observed for 0.5 mM TEMPONE and 1 mM $Au_{25}(SC3)_{18}{}^-$ in toluene under aerobic conditions (black) at 240 K. The red curve is the exponential fit to the data. The inset provides a schematic representation of the TREPR detection of $^1O_2$ generation through photoexcitation of the cluster.
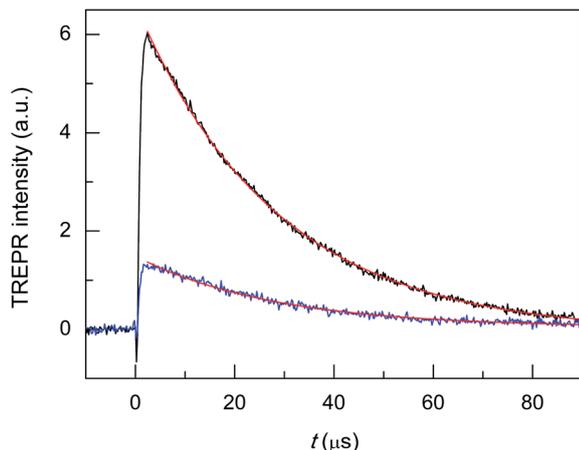
Fig. 5 TREPR transients observed under aerobic conditions for samples of 1 mM TPP and 0.5 (black) or 0.1 mM (blue) TEMPONE in toluene at 240 K. The corresponding exponential fits to the data are in red.

The best fit of the decay data obtained for $t > 3$ μs gives $k_\Delta = 3.54 \times 10^4$ s^{-1} ($r^2 = 0.999$), corresponding to a lifetime τ_Δ of 28.2(0.1) μs. This shows that TPP is, as expected, a very good photosensitizer. Comparison of this τ_Δ value with τ_Δ^S, however, evidences a relative τ decrease of 18.5%. To obtain information on a possible effect of TEMPONE as a quencher, we carried out further TPP photosensitization experiments in which the TEMPONE concentration was varied, as exemplified by the two traces in Fig. 5. We obtained: [TEMPONE] = 0.2 mM, $k_\Delta = 3.36 \times 10^4$ s^{-1}, and $\tau_\Delta = 29.8(0.4)$ μs; ([TEMPONE] = 0.1 mM, $k_\Delta = 3.66 \times 10^4$ s^{-1}, and $\tau_\Delta = 27.4(0.6)$ μs). The very similar τ_Δ values, therefore, show that under our experimental conditions the TEMPONE concentration does not affect the observed $^1O_2$ lifetime. Besides confirming that indeed TPP acts as a quencher, these results also indicate that despite the intense TREPR signals, TEMPONE polarization must involve a very small amount of $^1O_2$ present in solution. These tests validated the TREPR methodology and indicated that 0.5 mM TEMPONE could be consistently used with no detectable effect on the $^1O_2$ lifetime. The experiments described below were carried out under these conditions.

Tuning the photosensitizing properties of Au$_{25}$ nanoclusters

The TREPR data confirm that Au$_{25}$(SR)$_{18}^-$ can be used as a photosensitizer.[19] They also show that the $^1O_2$ lifetime measured in the presence of Au$_{25}$(SC3)$_{18}^-$ is much shorter than τ_Δ^S. The cluster is, therefore, not only a good sensitizer but also a good quencher, as observed for many sensitizers.[10] We will now specifically focus on this aspect. The decay of singlet oxygen can proceed by physical quenching, leading to deactivation of $^1O_2$, and chemical reactions, in which $^1O_2$ irreversibly reacts with some other species in solution.[10] In the presence of a generic molecule (M) capable of quenching or chemically reacting with $^1O_2$, eqn (4) must include further terms (eqn (5)):[10,56]

$$k_\Delta = k_{nr}[S] + k_r[S] + k_q[M] + k_{cr}[M] \qquad (5)$$

where k_q and k_{cr} are the second-order rate constants referring to the quenching and chemical reaction components, respectively. The gold nanoclusters do not react chemically with $^1O_2$. Although Au$_{25}$(SR)$_{18}^-$ may react with $^1O_2$ by electron transfer (ET), the effect of this reaction is detected only on a much longer time scale. For example, we found that flashing a Au$_{25}$(SC4)$_{18}^-$ sample (by using the same pulse sequence as in the TREPR experiments) in the presence of oxygen for 2 h transforms 8.8% of the anion into the corresponding neutral cluster (Fig. S3†). We can now thus focus only on the physical quenching paths, which consist of the first three terms in eqn (5). Physical quenching is the consequence of interactions with the solvent (terms k_{nr} and k_r) and solute/s (term k_q). For many solvents, including toluene, k_{nr} is dominant over k_r.[10] As to k_{nr}, solvent molecules deactivate singlet oxygen by electronic-vibrational energy transfer and by perturbing singlet oxygen with the result of facilitating its transition to $^3O_2$.[12,56] An effective physical quenching route is also attributed to the formation of a charge-transfer (CT) complex between singlet oxygen and the photosensitizer.[10,63,64] The resulting exciplex is a bimolecular excited state that can be described as a resonance of the excited and full ET states. The exciplex thus involves a partial (δ) CT[10] and its formation favors ISC[64–67] by providing a spin–orbit coupling contribution that helps overcoming the spin constrain associated with the $^1O_2 \rightarrow \, ^3O_2$ transition.[68] Exciplex formation is especially favored when the photosensitizer is a good electron-donating compound.[10] This is a condition that applies particularly well to Au$_{25}$(SR)$_{18}^-$ clusters, whose formal potential ($E°$) values (Au$_{25}$(SR)$_{18}^0$/Au$_{25}$(SR)$_{18}^-$ redox couple) are, compared with usual photosensitizers,[10] exceptionally low. In dichloromethane (DCM) containing 0.1 M tetrabutylammonium hexafluorophosphate (TBAH), which is the solvent/electrolyte system generally used to study and compare the electrochemical behavior of metal nanoclusters,[34] the $E°$ of, e.g., the Au$_{25}$(SC3)$_{18}^0$/Au$_{25}$(SC3)$_{18}^-$ redox couple is −0.171 V (298 K, potentials *versus* the saturated calomel electrode, SCE),[49] whereas that of O$_2$/O$_2^{-\bullet}$ is −0.85 V (this work).

The easiest way to tune the properties of Au$_{25}$ is to change the capping ligands. While this change does not affect the structure and the absorption spectrum,[18,69] other properties, especially the electrochemical potentials,[34,70] may change appreciably. Finally, the ligands provide a nanoenvironment surrounding the cluster core that determines the effective dielectric constant[70] and porosity of the capping monolayer,[69] and these factors may exert an influence on the quenching mechanisms of the excited states and ultimately the effective singlet-oxygen lifetime. To gain insights into this aspect, we compared the outcome of TREPR measurements carried out on Au$_{25}$ clusters capped by SC3, SC4, and SC2Ph thiolates. The ligand choice was primarily dictated by their ability to change the $E°$ of the Au$_{25}$(SR)$_{18}^0$/Au$_{25}$(SR)$_{18}^-$ redox couples quite significantly.[70,71]

Au$_{25}$(SC4)$_{18}^-$ and Au$_{25}$(SC2Ph)$_{18}^-$ display TREPR surfaces similar to that of Au$_{25}$(SC3)$_{18}^-$. Fig. 6 compares the reinforced absorptive-polarized transient signals observed upon $^1O_2$
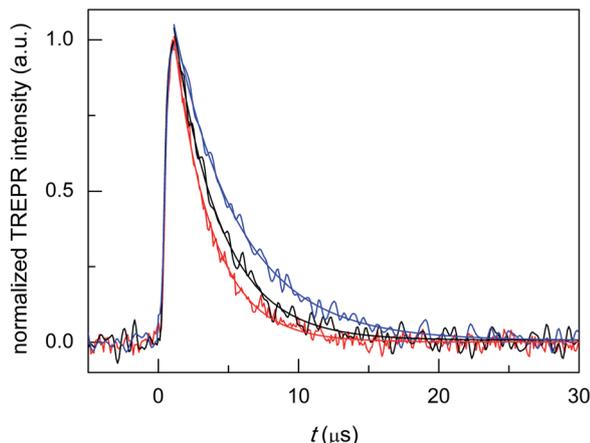
Fig. 6 TREPR (normalized) transients and corresponding exponential fits to the data for air-saturated toluene solutions of 0.5 mM TEMPONE and 1 mM $Au_{25}(SC4)_{18}^-$ (red), $Au_{25}(SC3)_{18}^-$ (black), and $Au_{25}(SC2Ph)_{18}^-$ (blue). Temperature = 240 K.

photosensitization by $Au_{25}(SC4)_{18}^-$, $Au_{25}(SC3)_{18}^-$, and $Au_{25}(SC2Ph)_{18}^-$ (red, black, and blue traces, respectively). The growth of the polarized signals occurs within 1 μs (that is, a bit faster than for TPP) and the maximum signal intensities are very similar, pointing to similar photosensitization efficiency (in Fig. 6 the intensities are normalized for the sake of better comparison of the transients).

Monoexponential fit to the decay data reveals small, yet clearly detectable differences in the value of k_Δ, which increases in the order $Au_{25}(SC2Ph)_{18}^-$ (2.17×10^5 s^{-1}, $r^2 = 0.990$) < $Au_{25}(SC3)_{18}^-$ (3.02×10^5 s^{-1}, $r^2 = 0.974$) < $Au_{25}(SC4)_{18}^-$ (3.69×10^5 s^{-1}, $r^2 = 0.986$); the corresponding lifetimes τ_Δ are 4.61(0.05), 3.31(0.05), and 2.71(0.04) μs, respectively. This order indeed matches that of the decreasing $E°$ of the anionic clusters (DCM/0.1 M TBAH, 298 K, E vs. SCE), which are −0.077, −0.171, and −0.188 V, respectively.[70,71] These data point to the ease of oxidation (lower $E°$ value) as an important factor enhancing the cluster quenching ability and are thus in keeping with the effect noted for other sensitizer families.[10]

Overall, these results evidence a detectable effect of the cluster oxidation potential on the singlet-oxygen decay kinetics and thus confirm an active role of the cluster also as a quencher. With alkanethiolate ligands, however, the potentials cannot be changed substantially.[34,70] A more substantial way to modify the physicochemical properties of gold nanoclusters is by doping their core with other metals. We thus focused on modifying $Au_{25}(SC4)_{18}^-$ to prepare the corresponding $Au_{24}M(SC4)_{18}^0$ clusters, with M = Hg, Cd. For these metals, monodoping is conveniently accomplished by carrying out the metal exchange on a preformed $Au_{25}(SR)_{18}^-$ cluster by using a salt or thiolate of the exogenous metal.[39,72–74] We focused on these two metals because they both dope the cluster on one of the icosahedron positions, as we could demonstrate very recently.[39] While in their neutral state, the resulting $Au_{24}M(SC4)_{18}^0$ clusters are diamagnetic and thus match the same magnetic state of anion $Au_{25}(SC4)_{18}^-$.

Monodoping affects the HOMO–LUMO gap. The values that can be estimated from the electrochemical peaks are:[39,70] Au, 1.30 eV; Hg, 1.28 eV; Cd, 1.41 eV. Similar differences are found for the optical bandgaps.[39,75] These differences are indeed noteworthy because, for example, a progressive change in the number of carbon atoms from 2 to 12 in $Au_{25}(SCn)_{18}$ does not affect the HOMO–LUMO gap, which remains constant at 1.30 eV.[70] Besides these differences, Hg and Cd doping affects the electrochemical potentials very significantly. In particular, the first oxidation of the $Au_{24}M(SC4)_{18}$ clusters occurs ($E°$ values) at −0.188 (Au), +0.364 (Hg), and +0.332 V (Cd).[39] In electrochemical terms, a positive shift of the first oxidation step by more than 0.5 V is indeed massive.

Hg doping induces remarkable changes in the TREPR transients (Fig. 7, black trace). First, in $Au_{24}Hg(SC4)_{18}^0$ the photosensitization efficiency is about two thirds that of $Au_{25}(SC4)_{18}^-$ (red trace). This decrease may be caused by a shorter triplet lifetime, a less efficient cluster-to-oxygen energy transfer to form singlet oxygen, or a lower quantum yield for the formation of the triplet. In this context, an important piece of information is provided in a recent study by Zhou *et al.* about the excited-state lifetime of similar (R = C2Ph) clusters, as the values determined for $Au_{24}Hg(SC2Ph)_{18}^0$ and $Au_{25}(SC2Ph)_{18}^-$ are 50 and 100 ns, respectively.[75] The observed TREPR intensities are indeed in rather good agreement with this ratio, and therefore, we may arguably conclude that the efficiency of singlet-oxygen generation is mainly determined by the cluster triplet lifetime. Regarding the hypothesis of a less efficient cluster-to-oxygen energy transfer, we note that the HOMO–LUMO gap of $Au_{24}Hg(SC4)_{18}^0$ (1.28 eV) is slightly smaller than for $Au_{25}(SC2Ph)_{18}^-$ (1.30 eV): the same should be true also for the corresponding triplet states and this may affect the cluster-oxygen energy transfer, although to a very small extent. Finally, ISC in the cluster should occur on a low ns timescale and very efficiently ($\Phi_T = 0.87$), as evaluated by Wen *et al.* for films of BSA-protected Au_{25} clusters.[76]
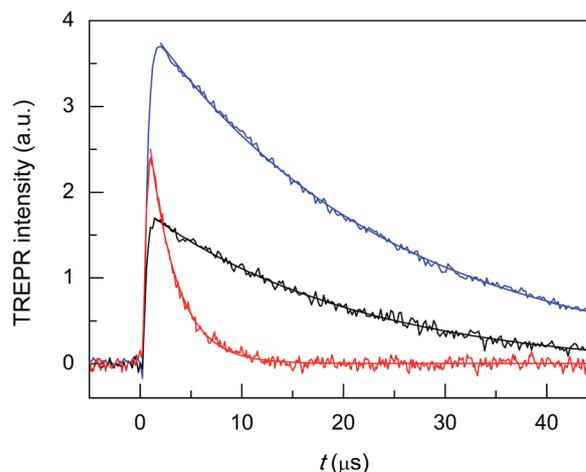

Fig. 7 Comparison of the TREPR transients and corresponding exponential fit to the data for air-saturated toluene solutions of 0.5 mM TEMPONE and 1 mM $Au_{24}Hg(SC4)_{18}^0$ (black), $Au_{24}Cd(SC4)_{18}^0$ (blue), and $Au_{25}(SC4)_{18}^-$ (red). Temperature = 240 K.

The most important effect brought about by the introduction of a single Hg atom, however, is to increase the singlet-oxygen lifetime by more than one order of magnitude: 19.5(0.2) ($k_\Delta = 5.13 \times 10^4$ s^{-1}, $r^2 = 0.990$) vs. 2.71 μs ($k_\Delta = 3.69 \times 10^5$ s^{-1}), which indicates that the mechanism of $^1O_2$ quenching is much less efficient than for the corresponding Au$_{25}$ cluster. Still, compared with the reference τ_Δ^S of 34.6 μs, the relative τ_Δ decrease is quite significant: 43.6%.

To make the cluster even more performing, the foreign-metal atom should minimize quenching effects without losing the photosensitization efficiency or possibly even increasing it with respect to Au$_{25}$. The doped cluster should, therefore, exhibit electrochemical properties similar to those of Au$_{24}$Hg(SC4)$_{18}^0$, a more significant population of the photogenerated triplet state, and ultimately, allow for a longer $^1O_2$ lifetime. A cluster that satisfies these requirements is Au$_{24}$Cd(SC4)$_{18}^0$, as it is almost as resistant toward oxidation as Au$_{24}$Hg(SC4)$_{18}^0$ (0.332 V vs. 0.364 V), its HOMO–LUMO gap is the largest of the three SC4 clusters, and according to Zhou et al.[75] its excited-state lifetime (in supposedly aerated solution) is 200 ns (R = C2Ph), i.e., two and four times longer than those of Au$_{25}$(SC2Ph)$_{18}^-$ and

Au$_{24}$Hg(SC2Ph)$_{18}^0$, respectively. In this regard, it is worth mentioning that TREPR (emission decay lifetime of 0.44(0.01) μs, $r^2 = 0.988$) points to a higher limit of ∼0.3 μs for the lifetime of the triplet of Au$_{24}$Cd(SC4)$_{18}^0$ under anaerobic conditions (Fig. S4†), as already noted and discussed for Au$_{25}$(SC3)$_{18}^-$. These general expectations of better performance are fully met: use of the Cd-doped cluster yields a longer singlet-oxygen lifetime ($k_\Delta = 4.31 \times 10^4$ s^{-1}, $r^2 = 0.999$, and $\tau_\Delta = 23.2(0.09)$ μs) than Au$_{24}$Hg(SC4)$_{18}^0$, a smaller relative τ_Δ decrease (32.9%) and a more significant photosensitization efficiency (Fig. 7, blue trace). In particular, the maximum intensity of the TREPR signals is ∼1.5 times larger than that observed for Au$_{25}$(SC4)$_{18}^-$ and more than two times larger than that of Au$_{24}$Hg(SC4)$_{18}^0$. The photosensitization efficiency of Au$_{24}$Cd(SC4)$_{18}^0$ is significant also in comparison with that of the TPP photosensitizer, as the TREPR signal intensity of the former is ∼1/2 that of TPP. The fact that the amount of triplet excited state obtained from Au$_{24}$Cd(SC4)$_{18}^0$ is quite significant is also supported by the presence of the negative spike for $t < 0.5$ μs, which, as already commented upon for TPP, is attributed to the Q-RTP component (eqn (1)).

Finally, we tested the Cd-doped cluster that has an even more positive oxidation potential, Au$_{24}$Cd(SC2Ph)$_{18}^0$, whose E° is 0.430 V (vs. 0.332 V for Au$_{24}$Cd(SC4)$_{18}^0$).[39] The DPV curves (oxidation region) of all clusters investigated and TPP are gathered in Fig. 8. Also for this cluster we estimate (Fig. S5:† TREPR emission decay lifetime of 0.44(0.01) μs, $r^2 = 0.989$) a higher limit of ∼0.3 μs for its triplet lifetime under anaerobic conditions. Indeed, the photosensitization outcome further improves (Fig. 9, blue trace), as the observed singlet-oxygen lifetime is even longer ($k_\Delta = 3.58 \times 10^4$ s^{-1}, $r^2 = 0.997$, and $\tau_\Delta = 27.9(0.25)$ μs). In particular, this τ_Δ value and the relative τ_Δ decrease, 19.3%, are virtually identical to those of TPP (Fig. 9, black trace), 28.2(0.1) μs and 18.5%, though the latter is more difficult to oxidize by as much as 0.563 V (Fig. 8). Besides the redox potentials, a comparison between the aforementioned estimated lifetime values (aerobic vs. anaerobic conditions)
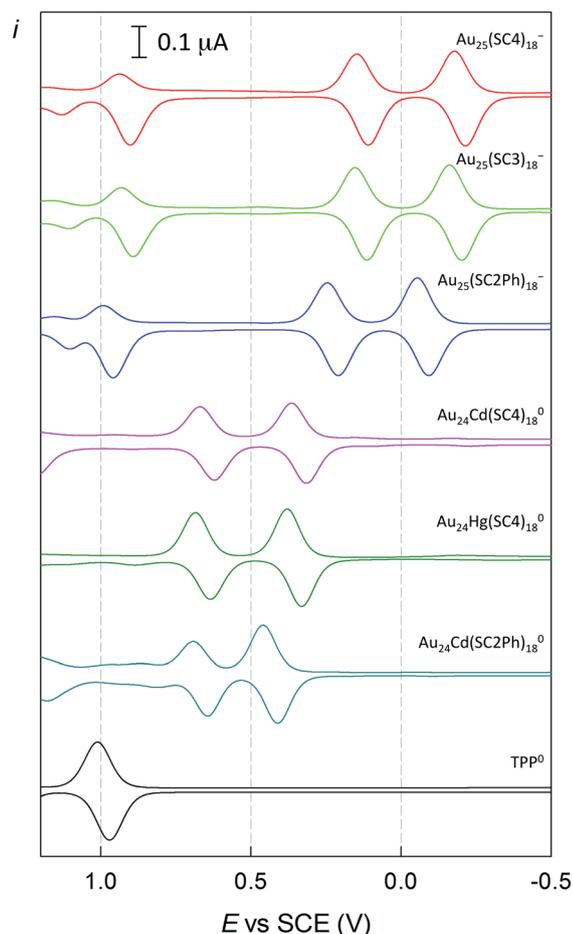

Fig. 8 Comparison between the DPV curves (oxidation region) of Au$_{25}$(SC4)$_{18}^-$, Au$_{25}$(SC3)$_{18}^-$, Au$_{25}$(SC2Ph)$_{18}^-$, Au$_{24}$Cd(SC4)$_{18}^0$, Au$_{24}$Hg(SC4)$_{18}^0$, Au$_{24}$Cd(SC2Ph)$_{18}^0$, and TPP. Glassy carbon electrode, DCM/0.1 M TBAH, and 25 °C.
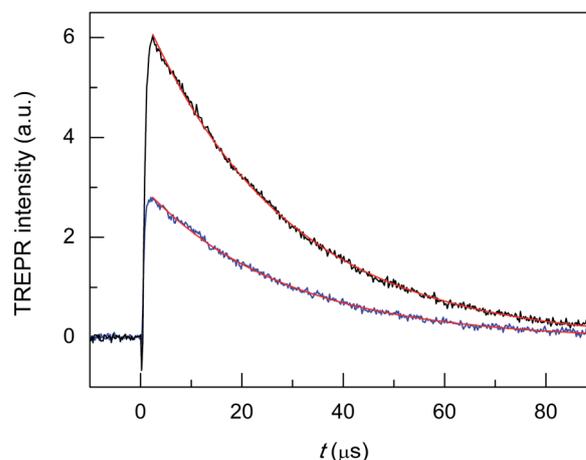

Fig. 9 TREPR transients and corresponding exponential fit to the data for air-saturated toluene solutions of 0.5 mM TEMPONE and 1 mM Au$_{24}$Cd(SC2Ph)$_{18}^0$ (blue) and TPP (black). Temperature = 240 K.

obtained for the Cd-doped clusters and TPP (whose triplet-state lifetime in the absence of oxygen increases by orders of magnitude)[13,62] shows that despite the much shorter intrinsic lifetime of their triplet state, the Cd-doped clusters are perfectly fine to accomplish the $^1O_2$ photosensitization job very efficiently.

Chemical quenching

To compare further the performance of doped and undoped clusters, we performed photosensitization experiments in the presence of 9,10-diphenylanthracene (DPA), which reacts with singlet oxygen to yield the endoperoxide 9,10-diphenyl-9,10-epidioxyanthracene (DPA-O$_2$) with rate constants on the order of 10^6 M^{-1} s^{-1}.[77] Its formation can be conveniently monitored through the decrease in the excitation and fluorescence spectra of DPA. Fig. 10 compares the fluorescence spectra of DPA in air-saturated toluene (at room temperature) containing the photosensitizer $Au_{24}Cd(SC4)_{18}{}^0$ (panel a) or $Au_{25}(SC4)_{18}{}^-$ (panel b) before and after 10 min pulsed irradiation (carried out as in the TREPR experiments) with a 532 nm laser at 240 K (for details, see the Experimental section).

For $Au_{24}Cd(SC4)_{18}{}^0$, the strong emission band of DPA at ~430 nm (excitation at 360 nm) is markedly quenched (by 56.9%), which confirms its particular efficiency as a photosensitizer. Instead, when $Au_{25}(SC4)_{18}{}^-$ is used as photosensitizer, only 13.6% quenching of the DPA emission is observed at ~430 nm. The different behavior of the two clusters is also quantitatively detected in the excitation spectra obtained at 450 nm: $Au_{24}Cd(SC4)_{18}{}^0$ causes a strong decrease of the absorption band of DPA (56.9%), whereas the variation is much less significant for $Au_{25}(SC4)_{18}{}^-$ (11.0%) (Fig. S6 and S7†). The absorption spectra of the solutions of the two clusters, which only show the optical features of the nanoclusters because their concentration is 100 times larger than that of DPA (the molar extinction coefficients of DPA,[78] $Au_{24}Cd(SC4)_{18}{}^0$, and $Au_{25}(SC4)_{18}{}^-$ are 1.4×10^4 M^{-1} cm^{-1} (372.5 nm), 4.68×10^4

M^{-1} cm^{-1} (398 nm) and 4.58×10^4 M^{-1} cm^{-1} (401 nm), respectively), exhibit no differences before and after laser irradiation (Fig. S8 and S9†), thereby pointing to their photostability (no change of the spectrum associated with cluster oxidation) under the given experimental conditions. These results thus show that $Au_{24}Cd(SC4)_{18}{}^0$ is a significantly better photosensitizer than $Au_{25}(SC4)_{18}{}^-$, in full agreement with the TREPR results.

Mechanism of physical quenching by Au$_{25}$ nanoclusters

The sequence of the observed τ_Δ values is in very good agreement with the cluster oxidation potentials (Fig. 11).

Due to the aforementioned considerations regarding k_r and k_{cr}, eqn (5) can be simplified to eqn (6):

$$k_\Delta = k_{nr}[S] + k_q[M] \tag{6}$$

k_q can thus be obtained from the k_Δ value determined experimentally and the $k_{nr}[S]$ term, which can be calculated from literature data[56] to be 2.89×10^4 s^{-1} at 240 K. According to the CT–ISC mechanism, the quenching process involving $^1O_2$ and the molecular Au nanocluster (M) can be summarized by using eqn (7)–(9):
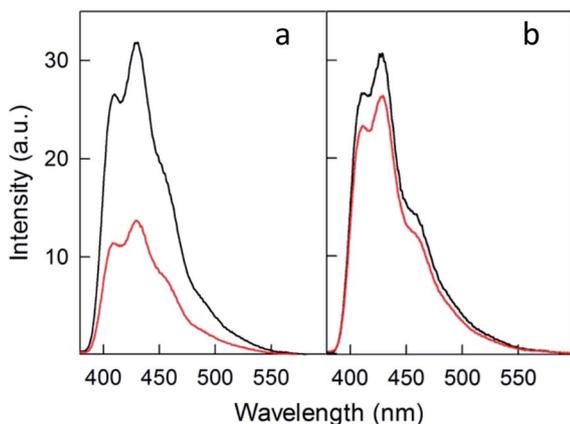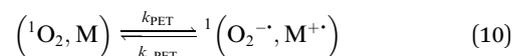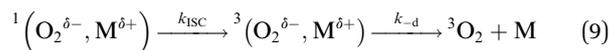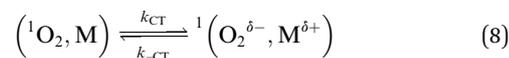
$$^1O_2 + M \underset{k_{-d}}{\overset{k_d}{\rightleftharpoons}} \left(^1O_2, M\right) \tag{7}$$

$$\left(^1O_2, M\right) \underset{k_{-CT}}{\overset{k_{CT}}{\rightleftharpoons}} {}^1\left(O_2{}^{\delta-}, M^{\delta+}\right) \tag{8}$$

$$^1\left(O_2{}^{\delta-}, M^{\delta+}\right) \overset{k_{ISC}}{\longrightarrow} {}^3\left(O_2{}^{\delta-}, M^{\delta+}\right) \overset{k_{-d}}{\longrightarrow} {}^3O_2 + M \tag{9}$$

$$\left(^1O_2, M\right) \underset{k_{-PET}}{\overset{k_{PET}}{\rightleftharpoons}} {}^1\left(O_2{}^{-\bullet}, M^{+\bullet}\right) \tag{10}$$
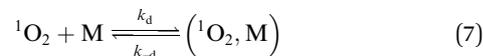
Fig. 10 Emission spectra (λ_{exc} = 360 nm) of 1.3×10^{-3} mM DPA in aerated toluene containing 0.13 mM (a) $Au_{24}Cd(SC4)_{18}{}^0$ or (b) $Au_{25}(SC4)_{18}{}^-$. The spectra correspond to before (black) and after 10 min irradiation (red) at 532 nm at 240 K. The spectra were obtained at room temperature.
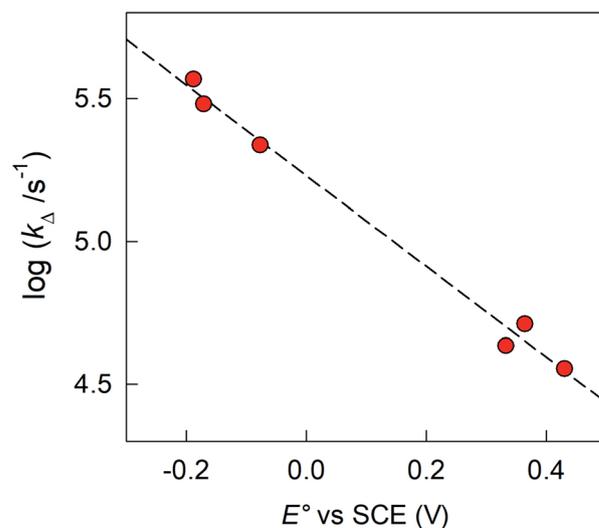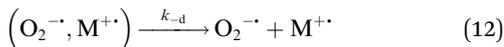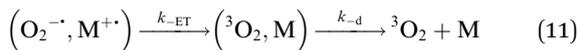
Fig. 11 Dependence of the $^1O_2$ decay rate constant k_Δ on the formal potentials for the oxidation of the clusters. The dashed line shows the linear fit to the data.

$$\left(O_2{}^{-\cdot}, M^{+\cdot}\right) \xrightarrow{k_{-ET}} \left({}^3O_2, M\right) \xrightarrow{k_{-d}} {}^3O_2 + M \qquad (11)$$

$$\left(O_2{}^{-\cdot}, M^{+\cdot}\right) \xrightarrow{k_{-d}} O_2{}^{-\cdot} + M^{+\cdot} \qquad (12)$$

where k_d and k_{-d} are the diffusion rate constants for the formation and dissociation of the caged species, k_{CT} and k_{-CT} are the forward and backward rate constants of the transfer of a partial charge δ between the caged ${}^1O_2$ and M species, and k_{ISC} is the rate constant for ISC in the exciplex. Reactions 10–12 can be competitive to the sequence 8–9 in quenching ${}^1O_2$: whereas k_{PET} and k_{-PET} are the forward and backward rate constants for the oxidation of the cluster by ${}^1O_2$ (that is, the possibility of re-crossing to the excited donor surface is included), k_{-ET} is the backward rate constant for the ET between M and ${}^3O_2$ (that is, charge recombination). It should be noted that eqn (7)–(12) are generically written for two neutral species. Whereas this is valid for the doped clusters, for $Au_{25}(SR)_{18}{}^-$ the negative charge of the cluster must be taken into account in eqn (7)–(12). The fact that the cluster may carry a charge does not prevent the formation of the exciplex, as shown very recently for a cationic excited state acceptor.[79] Charge-transfer activation of oxygen by both anionic and neutral gold nanoclusters has been described.[80,81] Very recent mass spectrometry results would indeed point to an effective interaction of oxygen and $Au_{25}(SC2Ph)_{18}{}^-$, at least in DCM.[82]

Charge-transfer induced quenching. We first focus on the quenching sequence 7–9 (the competition by the ET path, eqn (7) and (10)–(12), will be discussed later). Applying the steady-state approximation to the encounter complex and the singlet exciplex leads to the following expression (eqn (13)) for the k_q term in eqn (5):

$$k_q = \frac{k_d}{1 + \dfrac{k_{-d}}{k_{CT}} + \dfrac{k_{-d}}{k_{ISC}} \exp\!\left(\dfrac{\Delta G_{CT}^\circ}{RT}\right)} \qquad (13)$$

We start by considering $Au_{25}(SC4)_{18}{}^-$, which exhibits a less positive oxidation potential and the fastest quenching rate, and then we will discuss the differences caused by making the cluster oxidation more difficult. For this cluster, $k_\Delta = 3.69 \times 10^5$ s^{-1}. The term $k_q[M]$ can be obtained from eqn (6) by subtracting the rate constant for the intrinsic ${}^1O_2$ lifetime ($\tau_\Delta^S = 34.6$ μs and $k_\Delta^S = k_{nr}[S] = 2.89 \times 10^4$ s^{-1}). Hence, a value of $k_q = 3.40 \times 10^8$ M^{-1} s^{-1} is calculated using $[M] = 1$ mM.

The diffusion rate constants k_d and k_{-d} are estimated to be 1.9×10^{10} M^{-1} s^{-1} and 2×10^{10} s^{-1}, respectively (see the ESI†). The equilibrium constant K_{CT}, and thus ΔG_{CT}°, is unknown. However, ΔG_{CT}°, which refers to the transfer of the charge fraction δ, is conceivably related to ΔG_{ET}°,[10] which is the free energy for full ET between the cluster and singlet oxygen (eqn (10)). k_{CT} may be similarly estimated (eqn (14)) using a Marcus expression for the activation free energy $\Delta G_{CT}^\neq$ (eqn (15)).

$$k_{CT} = Z \exp[-\Delta G_{CT}^\neq / RT] \qquad (14)$$

$$\Delta G_{CT}^\neq = \Delta G_{0,CT}^\neq \left[1 + \left(\Delta G_{CT}^\circ \Big/ 4\Delta G_{0,CT}^\neq\right)\right]^2 \qquad (15)$$

The process is considered adiabatic and thus occurring at the contact distance between singlet oxygen and the cluster, as supported by recent results.[80–82] The frequency factor Z is estimated (see the ESI†) by taking into account the role of solvent friction in determining the rate of crossing the barrier.[83] $\Delta G_{0,CT}^\neq$ is the intrinsic barrier, that is, the value of $\Delta G_{CT}^\neq$ at zero driving force. In analogy to the ET intrinsic barrier ($\Delta G_{0,ET}^\neq$), $\Delta G_{0,CT}^\neq$ can be seen as composed of a solvent reorganization term, $\Delta G_{0,s,CT}^\neq$, and an inner component, $\Delta G_{0,i,CT}^\neq$, which describes the molecular deformation of bond lengths and angles of the reacting system. For a full ET,[84,85] $\Delta G_{0,ET}^\neq$ can be calculated from the homogeneous self-exchange $(\Delta G_{0,ET}^\neq)_{hom,ex}$ values of the two redox couples (here, $M^{+\cdot}/M$ and ${}^1O_2/O_2{}^{-\cdot}$) (eqn (16)):

$$\Delta G_{0,ET}^\neq = \left[\left(\Delta G_{0,ET}^\neq\right)_{hom,ex,M^{+\cdot}/M} + \left(\Delta G_{0,ET}^\neq\right)_{hom,ex,O_2/O_2{}^{-\cdot}}\right] \Big/ 2 \qquad (16)$$

The values of the two $(\Delta G_{0,ET}^\neq)_{hom,ex}$ terms can be obtained from the corresponding heterogeneous intrinsic barriers through eqn (17):[86]

$$(\Delta G_0^\neq)_{hom,ex} = 2(\Delta G_0^\neq)_{het} - (\Delta G_{0,s}^\neq)_{hom,ex} \qquad (17)$$

where $(\Delta G_{0,s}^\neq)_{hom,ex}$ is the homogeneous solvent reorganization term. For the cluster, we use the electrochemical $(\Delta G_{0,ET}^\neq)_{het} = 0.222$ eV, which was previously obtained in DCM/0.1 M TBAH, at 298 K from the standard heterogeneous rate constant.[69] For ${}^1O_2/O_2{}^{-\cdot}$ and assuming that the intrinsic barriers of ${}^1O_2/O_2{}^{-\cdot}$ and ${}^3O_2/O_2{}^{-\cdot}$ are the same, we obtain $(\Delta G_{0,ET}^\neq)_{het} = 0.408$ eV by cyclic-voltammetry analysis of the oxygen reduction peak (see the Experimental section). To estimate these parameters for toluene at 240 K and then calculate the other terms of eqn (17), we followed a procedure described in the ESI.† For the ${}^1O_2/Au_{25}(SC4)_{18}{}^-$ system, the use of eqn (16) yields $\Delta G_{0,ET}^\neq = 0.23$ eV. It is worth mentioning that for DCM at 298 K, $\Delta G_{0,ET}^\neq$ is much larger, 0.40 eV: this is a consequence of the fact that the very low polarity of toluene makes the solvent reorganization term very small, with the result that the already significant inner reorganization of Au_{25} clusters[69–71,87] and possibly oxygen[88] becomes largely dominant (85%). For this reason, we can neglect that for $(\Delta G_{0,ET}^\neq)_{het}$ (and thus $(\Delta G_0^\neq)_{hom,ex}$) the radii employed in the solvent reorganization calculations are correct, whereas $(\Delta G_0^\neq)_{ET}$ might be slightly affected by the penetration of ${}^1O_2$ inside the monolayer, as the effective cluster radius should be a bit smaller. A posteriori, we checked that this assumption is indeed valid for the CT–ISC mechanism even if one uses for the cluster just the crystallographic radius of the gold core (4.9 Å).[70]

Both k_{CT} and K_{CT} require calculating ΔG_{ET}° and how to relate it to ΔG_{CT}°. Additionally, k_{CT} requires converting $\Delta G_{0,ET}^\neq$ into $\Delta G_{0,CT}^\neq$. For ${}^1O_2$ quenching, ΔG_{CT}° is usually taken as a fraction f of ΔG_{ET}° to account for the partial character δ of ET in the

formation of the exciplex.[10] ΔG_{ET}° can be estimated, according to Rehm and Weller,[89,90] with eqn (18). Because the process here considered involves a neutral and a charged species, $^{1}O_2/$ Au$_{25}$(SC4)$_{18}^{-}$, the coulombic term associated with the formation of charges is zero. To avoid confusion, the actual charge of the Au$_{25}$ cluster is made explicit.

$$\Delta G_{ET}^{\circ} = nFE^{\circ}\left(M^{\bullet}/M^{-}\right) - nFE^{\circ}\left(O_2/O_2^{-\bullet}\right) - E_{exc} \qquad (18)$$

where n is the number of exchanged electrons (for a full ET, $n = 1$), F is the Faraday constant, $E^{\circ}(M^{\bullet}/M^{-})$ and $E^{\circ}(O_2/O_2^{-\bullet})$ are the formal potentials of the $M^{\bullet}/M^{-}$ and oxygen/superoxide redox couples, respectively, and $E_{exc} = 94$ kJ mol^{-1} is the $^{3}\Sigma_g^{-}$ to $^{1}\Delta_g$ excitation energy. Eqn (18) (also in its form including the coulombic term) provides a reasonable estimate of ΔG_{ET}°, and therefore, $E^{\circ}(^{1}O_2/O_2^{-\bullet})$ will be taken as $E^{\circ}(O_2/O_2^{-\bullet}) - E_{exc}/F = -0.850 + 0.974 = 0.124$ V (for details, see the ESI†).

As to the fraction f of ΔG_{ET}°, it has been proposed that $\delta \sim f^{1/2}$, as inferred from experimental trends involving neutral donors.[10] Because of the charge here involved, however, we will use a linear dependence (eqn (19)) in which δ simply replaces $n = 1$ in eqn (18). Hence:

$$\Delta G_{CT}^{\circ} = \delta F\left[E^{\circ}\left(M^{\bullet}/M^{-}\right) - E^{\circ}\left(^{1}O_2/O_2^{-\bullet}\right)\right] \qquad (19)$$

Regarding the conversion of $\Delta G_{0,ET}^{\neq}$ into $\Delta G_{0,CT}^{\neq}$, we consider that $\Delta G_{0,s,CT}^{\neq}$ should also depend on the square of δ, whereas $\Delta G_{0,i,CT}^{\neq}$ has been previously considered as, possibly, independent of it, although differences were noted between different classes of compounds.[91] The actual dependence of $\Delta G_{0,CT}^{\neq}$ on δ is indeed unclear, especially in solvents of a very low dielectric constant and/or when $\Delta G_{0,i,CT}^{\neq}$ is dominant, as noted above for Au$_{25}$ clusters.[69–71,87] Here, to balance contributions, we will consider a simple linear dependence, $\Delta G_{0,CT}^{\neq} \sim \delta \Delta G_{0,ET}^{\neq}$.

k_{CT} can now be obtained from the appropriate preexponential factor (eqn (14) and S1,† with $Z = 4.6 \times 10^{10}$ s^{-1}), provided that a reasonable δ value is used in eqn (19). As δ is unknown, we will follow an approach similar to that used for other series of photosensitizers.[10,66,67] In ETs, the transfer coefficient α is introduced to describe how the activation free energy responds to changes in the reaction driving force, that is, $\alpha = d\Delta G_{ET}^{\neq}/d\Delta G_{ET}^{\circ} = -RTd \ln k_{ET}/d\Delta G_{ET}^{\circ}$. Because of the quadratic expression relating $\Delta G_{ET}^{\neq}$ to ΔG_{ET}°, α is expected to be 0.5 at zero driving force.[85] We will focus on the three Au$_{25}$ clusters, which are self-consistent in terms of cluster charge. The corresponding driving forces for ET (eqn (18)) range from -0.312 (SC4) to -0.201 (SC2Ph) eV, that is, these processes are exergonic, yet not too far from $\Delta G_{ET}^{\circ} = 0$. The corresponding log k_q vs. ΔG_{ET}° plot provides a slope corresponding to a very small α value of 0.10. Adjusting δ in eqn (19) shows that $\alpha \sim 0.5$ is obtained when $\delta = 0.2$. This figure corresponds to ΔG_{CT}° values ranging from -0.06 to -0.04 eV. This value of δ is indeed quite similar to those previously proposed for $^{1}O_2$ quenching by other photosensitizers.[10,66,67] We also should note that δ is expected to decrease for more positive reaction free energies.[79] Using $\delta = 0.2$, the remaining quantities in eqn (13) are defined. Hence, an experimental rate constant (SC4) of $k_q = 3.40 \times 10^8$

M^{-1} s^{-1} corresponds to $\Delta G_{CT}^{\circ} = -0.062$ eV, $k_{CT} = 1.8 \times 10^{10}$ s^{-1}, and $k_{ISC} = 1.8 \times 10^{7}$ s^{-1}. For common photosensitizers, ISC is a fast process, with rate constant values estimated to be $\sim 10^{10}$ s^{-1}.[66] Despite the several inputs and assumptions and the resulting comparatively small k_{ISC} value, this kinetic analysis would suggest that the same CT–ISC mechanism proposed for $^{1}O_2$ quenching by other photosensitizers is plausible. Different assumptions on the preexponential factor Z do not affect the value of k_{ISC}, as already observed.[66]

Electron-transfer induced quenching. On the other hand, Au$_{25}$ clusters provide unusually[92] negative free energies for ET. This new situation may indeed make the reactions (10)–(12) competitive to reactions (8) and (9). As a matter of fact, we already noted that some oxidation of the Au$_{25}$(SC4)$_{18}^{-}$ cluster takes place, which points to the occurrence of reaction (12). Although mechanistically useful, however, this reaction only occurs on a long time scale, and therefore, is not kinetically relevant in consuming the charge-separated pair formed in reaction (10). The quantities already estimated allow us to estimate the likeliness of this competition/alternative path. Thus, assuming that only the ET (indicated as photoinduced ET, PET, to distinguish it from the ET in eqn (11)) mechanism (eqn (7), (10) and (11)) is responsible for $^{1}O_2$ quenching, the following expression (eqn (20)) for k_q ensues:

$$k_q = \frac{k_d}{1 + \dfrac{k_{-d}}{k_{PET}} + \dfrac{k_{-d}}{k_{-ET}} \exp\left(\dfrac{\Delta G_{PET}^{\circ}}{RT}\right)} \qquad (20)$$

where the steady-state approximation has been applied to the encounter complex and the charge-separated pair. The resulting relevant rate constants are $k_{PET} = 3.9 \times 10^8$ s^{-1} and $k_{-ET} = 2.0 \times 10^{10}$ s^{-1}. Both ETs can be considered as irreversible because the corresponding k_{-PET} and k_{ET} are 1.1×10^2 and 2.5×10^{-4} s^{-1}, respectively, and thus escape from the cage is much faster. In other words, the third term in the denominator of eqn (20) is orders of magnitude smaller than the first two terms (1 and 51.3, respectively). The process described in eqn (11) is thus essentially rate limited by k_{PET} and corresponds to an ET-induced ISC. Because of the many assumptions involved, all these rate-constant values should be considered only as estimates. Nonetheless, we note that the resulting k_q of 3.6×10^8 s^{-1} is in full agreement with the actual k_q (assuming that only eqn (7) and (10) are kinetically relevant), and this points to the full ET–ISC sequence as the most probable mechanism, although some contribution from the CT–ISC mechanism cannot be excluded. Different assumptions on the preexponential factor, making it larger, would make k_{PET} exceedingly large. If one now considers Au$_{25}$(SC2Ph)$_{18}^{-}$, which of the three Au$_{25}$ clusters is the one exhibiting the most positive oxidation potential, the picture does not change much and similar conclusions can be reached.

It is worth making a comment about the spin constrains. For this ET pathway, the singlet-triplet spin transition rate might affect the overall back ET rate in eqn (11). Indeed, spin-forbidden transitions can be orders of magnitude slower than the corresponding allowed transition.[93] Both caged species

formed in eqn (10) are radicals and the exchange interaction between them gives rise to nondegenerate singlet and triplet states (spin-correlated radical pair). In the present case, the singlet state has a higher energy and, as the precursor is a singlet ($^1O_2$), it is initially more populated. Therefore, the back ET rate constant should be considered as an upper limit. However, the rate is still large enough to make $^3O_2$ formation a very rapid step.

Quenching by the doped clusters. Regarding the doped clusters, the ΔG°_{ET} in eqn (18) (with $E^\circ(M^{+\cdot}/M)$ in place of $E^\circ(M^\cdot/M^-)$) requires adding the coulombic term, as now two opposite charges form. This correction can be performed for CT according to Rhem–Weller,[89,90] who considered this term as negative (stabilization of the opposite charges) (eqn (21)):

$$\Delta G^\circ_{CT} = \delta F\left[E^\circ(M^{+\cdot}/M) - E^\circ(^1O_2/O_2^{-\cdot})\right]$$
$$+ (+\delta)(-\delta)e^2/4\pi\varepsilon_s\varepsilon_0 a \qquad (21)$$

where e is the charge of the electron and a is the distance between the two species (usually taken as the sum of the two radii, assuming that the species as spherical). The larger the δ and the smaller the ε_s, the larger the negative contribution to ΔG°_{CT}. For photoinduced ETs, coulombic stabilization has been shown to be especially important for dielectric constants smaller than 13.[94]

It is useful to compare TPP and $Au_{24}Cd(SC2Ph)_{18}{}^0$, which exhibit very similar k_q values of 6.5×10^6 and 6.9×10^6 M^{-1} s^{-1}, respectively. For TPP, the decrease of ΔG°_{CT} caused by the coulombic term depends on the value of δ: for example, it is 0.032 and 0.008 eV for $\delta = 0.2$ and 0.1, respectively. In the absence of further information, however, we will keep using $\delta = 0.2$. The CT–ISC path can reproduce the experimental k_q value when k_{ISC} is set to 2.4×10^{10} s^{-1}, which is indeed a reasonable value for a molecular system such as TPP.[66] For the sake of argument, the use of a very small δ value of 0.1 would lower k_{ISC} to 7.5×10^8 s^{-1}. Regardless, there is no competition from the ET path (eqn (10) and (11)), as k_{PET} drops by several orders of magnitude.

For $Au_{24}Cd(SC2Ph)_{18}{}^0$, the situation is more intriguing. Reproducing the observed k_q value, requires $k_{ISC} = 3.7 \times 10^7$ s^{-1}, which, if one considers the error introduced by the various approximations, is probably the same as that calculated for $Au_{25}(SC4)_{18}{}^-$. On the other hand, the independently estimated k_{PET}, 3.2×10^6 s^{-1}, leads (eqn (20)) to $k_q = 5.3 \times 10^6$ M^{-1} s^{-1}, which is also comparable to the experimental value of 6.9×10^6 M^{-1} s^{-1}. We are thus facing the same mechanistic competition addressed for the undoped Au_{25} clusters.

Conclusions

Diamagnetic $Au_{24}M(SR)_{18}$ clusters are shown to be effective singlet-oxygen photosensitizers. As to their efficiency as singlet-oxygen quenchers, we show that it can be modulated quite precisely by changing the ligands and/or one of the Au atoms. The use of very sensitive TREPR spectroscopy allowed us to determine $^1O_2$ lifetimes ranging from 2.71 to 27.9 μs. The latter,

which was measured for $Au_{24}Cd(SC2Ph)_{18}{}^0$, is virtually the same as that of TPP, a well-known reference photosensitizer.

Analysis of the results leads to three main conclusions.

(1) We have described the first kinetic analysis of the quenching mechanism/s by gold nanoclusters. The Au_{25} clusters have unusually low E° values, yielding almost unprecedented[92] negative ΔG°_{ET} values. $^1O_2$ quenching involves both CT–ISC and ET–ISC mechanisms, although the latter appears to be the most probable: indeed, for the ET–ISC mechanism the k_q value is fully calculated according to eqn (20), whereas for the CT–ISC mechanism the k_{ISC} is adjusted to reproduce the experimental k_q value via eqn (13). Therefore, the actual k_{ISC} might be even smaller. This is also supported by the fact that $^1O_2$ quenching by the corresponding $Au_{24}M$ doped clusters also appears to be possible through both mechanisms. The ET–ISC mechanism is made possible because the substantially more positive E° values of these doped clusters are largely compensated by the coulombic term (eqn (21)). This would imply that the use of a more polar solvent, which decreases the value of the coulombic term[89,90] and may even revert its sign,[94] would remove the feasibility of the ET–ISC mechanism, leaving CT–ISC as the only plausible quenching mechanism.

(2) Despite the possibility of quenching $^1O_2$ through two mechanisms, we have detected the striking effect that the k_{ISC} values estimated for the nanoclusters are consistently smaller than those estimated for other molecular systems (and here shown for TPP) by *no less than two orders of magnitude*. This observation is obviously beneficial in terms of using this family of nanoclusters as $^1O_2$ photosensitizers with minimum $^1O_2$ quenching efficacy and makes these materials extremely promising for practical applications. Indeed, this large difference in k_{ISC} values points to something special in the interaction between nanoclusters and $^1O_2$. Minaev concluded that, to achieve an efficient intersystem crossing enhancement, there should be a non-linear encounter geometry between $^1O_2$ and the quencher molecular axes.[68,93] This condition is typically fulfilled for common molecules, as quenching can be treated as a series of random encounters. Instead, ligand-protected gold nanoclusters are composed of a hard core and a dynamic capping layer,[69] which is a feature not present in regular molecules. When inside the monolayer, interactions of $^1O_2$ with the ligands may give rise to orientation-specific interactions with the Au orbitals. In this framework, our results would suggest that an approximately axial collision takes place, as this orientation, according to Minaev, does not lead to strong ISC. More generally, it is conceivable that the limited orientations imposed by the capping monolayer can make ISC substantially less favored than in common molecular systems, where all relative orientation geometries and, therefore, ISC contributions are possible.

(3) The sequence of the observed τ_Δ values illustrated in Fig. 11 demonstrates that the efficiency of $Au_{24}M(SR)_{18}$ clusters as a singlet oxygen quencher is a function of their E° value. We thus expect that a more positive E° would allow us to obtain even better results and possibly reach the physiological limit of

$\tau_\Delta^S = 34.6$ μs, $i.e.$, no physical quenching by the cluster. According to Fig. 11, whose linear fit has a good r^2 value of 0.990, the "ideal" cluster should have an oxidation potential at least more positive than $\sim$0.5 V $vs.$ SCE in DCM/0.1 M TBAH. We believe that this target is indeed reachable through proper selection of the ligands to cap a cluster of the $Au_{24}Cd(SR)_{18}^0$ family, which also appears to have the longest triplet lifetime.

These results, methodologies, insights, and conclusions are expected to provide further ideas and incentive for using atomically precise gold nanoclusters as efficient photosensitizers, which is a topic of current interest for both fundamental and applied research.[95,96]

Experimental

TREPR

For the TREPR measurements, a pulsed laser beam from a Nd:YAG laser (Quantel Brilliant, pulse length 5 ns, pulse energy 5 mJ, and pulse repetition rate 20 Hz) was used for the optical excitation of the samples at 532 nm. At this wavelength, the absorption of all $Au_{24}M(SR)_{18}$ clusters is significantly larger than for nitroxides. The measurements were carried out by using a Bruker ER200D (X-band) spectrometer with an extended detection bandwidth (6 MHz), disabling the magnetic field modulation and working in a direct detection mode. The temperature of the sample inside the EPR cylindrical cavity (8 mm optical access) was controlled to 240 K by using a variable-temperature nitrogen flow system. The time-dependent EPR signals were digitized using a digital oscilloscope (LeCroy Model LT344) with a maximum acquisition rate of 500 megasample/s synchronized with the laser pulse. The time resolution of the instrument was $\sim$150 ns. Data collection was performed with a personal computer and software that allowed controlling the magnetic field and setting the digital oscilloscope. Typically, 300 transient signals were averaged under on-resonance conditions and subtracted from those accumulated off-resonance to eliminate the background signal induced by the laser pulse. A complete two-dimensional data set that shows the EPR signal as a function of both time and magnetic field consists typically of a set of transient signals, containing 500 points each, recorded at 128 different magnetic field positions. The 500×128 matrix gave a two-dimensional time/field data set from which the transient spectra were extracted.

Electrochemistry

The DPV and CV measurements were carried out in DCM/0.1 M TBAH, under an Ar atmosphere, in a glass cell, at 25 °C. For DPV we used a CHI 660c electrochemical workstation, whereas for the electrode kinetics, CV experiments we used an EG&G-PARC 173/179 potentiostat-digital coulometer, an EG&G-PARC 175 universal programmer, and a Nicolet 3091 12-bit resolution digital oscilloscope. The working electrode was a glassy carbon microdisk (9.1×10^{-4} cm^2), prepared and activated as already described.[97] The counter electrode was a Pt wire. A silver wire, which was kept in a tube filled with the same electrolyte solution and separated from the main compartment by a Vycor frit, served as a quasi-reference electrode. At the end of the experiments, its potential was calibrated after addition of ferrocene; the ferricenium/ferrocene redox couple has $E° = 0.460$ V (SCE) in DCM/0.1 M TBAH. All potential values are reported against the SCE. Standard DPV parameters were employed: peak amplitude = 50 mV, pulse width = 0.05 s, increments per cycle = 2 mV, and pulse period = 0.1 s. For CV, we applied positive feedback correction to minimize the ohmic drop between the working and the reference electrodes. The standard heterogeneous rate constant, k_{het}°, for oxygen reduction on a glassy carbon electrode was determined by the analysis of the CVs obtained at various scan rates (v). In DCM/TBAH 0.1 M, the separation between the cathodic and anodic peak potentials is large also at low v values ($e.g.$, 0.228 V at 0.2 V s^{-1}) pointing to a small k_{het}° value. The latter was determined by digital simulation of the experimental CVs. For digital simulation, we used DigiSim 3.03 software, using a step size of 1 mV and an exponential expansion factor of 0.5.

Author contributions

M. A. carried out most of the TREPR measurements and analyses; W. F. prepared and characterized all clusters; S. A. carried out the electrochemical experiments; M. A., T. D. and S. B. conducted the chemical quenching experiments; A. Z. and M. R. contributed to the TREPR study; S. A. and F. M. carried out the kinetic analysis; M. R. and F. M. designed the research; M. A., S. A., M. R., and F. M. wrote the paper.

Conflicts of interest

There are no conflicts to declare.

Acknowledgements

References

1 K. H. Becker, W. Groth and U. Schurath, *Chem. Phys. Lett.*, 1971, **8**, 259–262.

2 (*a*) F. Wilkinson, W. P. Helman and A. B. Ross, *J. Phys. Chem. Ref. Data*, 1995, **24**, 663–1021; (*b*) F. Wilkinson and J. G. Brummer, *J. Phys. Chem. Ref. Data*, 1981, **10**, 809–999.

3 M. Ruzzi, E. Sartori, A. Moscatelli, I. V. Khudyakov and N. J. Turro, *J. Phys. Chem. A*, 2013, **117**, 5232–5240.

4 I. Amato, *Science*, 1993, **262**, 32–33.

5 A. Greer, *Acc. Chem. Res.*, 2006, **39**, 797–804.

6 N. J. Turro, V. Ramamurthy and J. C. Scaiano, Molecular Oxygen and Organic Photochemistry, in *Modern Molecular Photochemistry of Organic Molecules*, University Science Books, Sausalito, 2010, ch. 14, pp. 1001–1042.

7 A. A. Ghogare and A. Greer, *Chem. Rev.*, 2016, **116**, 9994–10034.

8 Y. Nosaka and A. Y. Nosaka, *Chem. Rev.*, 2017, **117**, 11302–11336.

9 D. E. Dolmans, D. Fukumura and R. K. Jain, *Nat. Rev. Cancer*, 2003, **3**, 380–387.

10 C. Schweitzer and R. Schmidt, *Chem. Rev.*, 2003, **103**, 1685–1757.

11 P. R. Ogilby, *Chem. Soc. Rev.*, 2010, **39**, 3181–3209.

12 M. Bregnhøj, M. Westberg, B. F. Minaev and P. R. Ogilby, *Acc. Chem. Res.*, 2017, **50**, 1920–1927.

13 M. C. DeRosa and R. J. Crutchley, *Coord. Chem. Rev.*, 2002, **233–234**, 351–371.

14 J. R. Hurst, J. D. McDonald and G. B. Schuster, *J. Am. Chem. Soc.*, 1982, **104**, 2065–2067.

15 P. R. Ogilby and C. S. Foote, *J. Am. Chem. Soc.*, 1983, **105**, 3423–3430.

16 A. A. Krasnovsky Jr, M. E. Bashtanov, N. N. Drozdova, O. A. Yuzhakova and E. A. Luk'yanets, *Quantum Electron.*, 2002, **32**, 83–86.

17 Y. You, *Org. Biomol. Chem.*, 2018, **16**, 4044–4060.

18 R. Jin, C. Zeng, M. Zhou and Y. Chen, *Chem. Rev.*, 2016, **116**, 10346–10413.

19 H. Kawasaki, S. Kumar, G. Li, C. Zeng, D. R. Kauffman, J. Yoshimoto, Y. Iwasaki and R. Jin, *Chem. Mater.*, 2014, **26**, 2777–2788.

20 M. Sakamoto, T. Tachikawa, M. Fujitsuka and T. Majima, *Langmuir*, 2009, **25**, 13888–13893.

21 T. Das, P. Ghosh, M. S. Shanavas, A. Maity, S. Mondal and P. Purkayastha, *Nanoscale*, 2012, **4**, 6018–6024.

22 J. Y. Zhao, R. Cui, Z. L. Zhang, M. Zhang, Z. X. Xie and D. W. Pang, *Nanoscale*, 2014, **6**, 13126–13134.

23 R. Vankayala, C. L. Kuo, K. Nuthalapati, C. S. Chiang and K. C. Hwang, *Adv. Funct. Mater.*, 2015, **25**, 5934–5945.

24 D. Yang, G. Yang, S. Gai, F. He, G. An, Y. Dai, R. Lv and P. Yang, *Nanoscale*, 2015, **7**, 19568–19578.

25 M. Yamamoto, I. Osaka, K. Yamashita, H. Hasegawa, R. Arakawa and H. Kawasaki, *J. Lumin.*, 2016, **180**, 315–320.

26 M. Yamamoto, K. Shitomi, S. Miyata, H. Miyaji, H. Aota and H. Kawasaki, *J. Colloid Interface Sci.*, 2018, **510**, 221–227.

27 S. Miyata, H. Miyaji, H. Kawasaki, M. Yamamoto, E. Nishida, H. Takita, T. Akasaka, N. Ushijima, T. Iwanaga and T. Sugaya, *Int. J. Nanomed.*, 2017, **12**, 2703–2716.

28 D. Hikosou, S. Saita, S. Miyata, H. Miyaji, T. Furuike, H. Tamura and H. Kawasaki, *J. Phys. Chem. C*, 2018, **122**, 12494–12501.

29 R. Ho-Wu, S. H. Yau and T. Goodson III, *J. Phys. Chem. B*, 2017, **121**, 10073–10080.

30 G. Zhang, R. Wang and G. Li, *Chin. Chem. Lett.*, 2018, **29**, 687–693.

31 J. Zhang, Z. Li, J. Huang, C. Liu, F. Hong, K. Zheng and G. Li, *Nanoscale*, 2017, **9**, 16879–16886.

32 Z. Li, C. Liu, H. Abroshan, D. R. Kauffman and G. Li, *ACS Catal.*, 2017, **7**, 3368–3374.

33 K. Kawamura, D. Hikosou, A. Inui, K. Yamamoto, J. Yagi, S. Saita and H. Kawasaki, *J. Phys. Chem. C*, 2019, **123**, 26644–26652.

34 S. Antonello and F. Maran, *Curr. Opin. Electrochem.*, 2017, **2**, 18–25.

35 (a) M. Agrachev, S. Antonello, T. Dainese, M. Ruzzi, A. Zoleo, E. Aprà, N. Govind, A. Fortunelli, L. Sementa and F. Maran, *ACS Omega*, 2017, **2**, 2607–2617; (b) M. Agrachev, S. Antonello, T. Dainese, M. Ruzzi, A. Zoleo, E. Aprà, N. Govind, A. Fortunelli, L. Sementa and F. Maran, Correction to Magnetic Ordering in Gold Nanoclusters, *ACS Omega*, 2017, **2**, 3595.

36 M. Agrachev, M. Ruzzi, A. Venzo and F. Maran, *Acc. Chem. Res.*, 2019, **52**, 44–52.

37 J. F. Parker, C. A. Fields-Zinna and R. W. Murray, *Acc. Chem. Res.*, 2010, **43**, 1289–1296.

38 X. Kang, H. Chong and M. Zhu, *Nanoscale*, 2018, **10**, 10758–10834.

39 W. Fei, S. Antonello, T. Dainese, A. Dolmella, M. Lahtinen, K. Rissanen, A. Venzo and F. Maran, *J. Am. Chem. Soc.*, 2019, **141**, 16033–16045.

40 A. Kawai, M. Mitsui, Y. Kobori and K. Obi, *Appl. Magn. Reson.*, 1997, **12**, 405–410.

41 C. G. Martinez, S. Jockusch, M. Ruzzi, E. Sartori, A. Moscatelli, N. J. Turro and A. L. Buchachenko, *J. Phys. Chem. A*, 2005, **109**, 10216–10221.

42 C. Corvaja, in *Fullerenes: From Synthesis to Optoelectronic Properties*, ed. D. M. Guldi and N. Martin, Kluwer Academic Publishers, 2002, pp. 213–236.

43 C. Blättler, F. Jent and H. A. Paul, *Chem. Phys. Lett.*, 1990, **166**, 375–380.

44 K. M. Salikhov, Yu. N. Molin, R. Z. Sagdeev and A. L. Buchachenko, *Spin Polarization and Magnetic Effects in Radical Reactions*, Elsevier, Amsterdam, 1984.

45 M. Mitsui, K. Takeda, Y. Kobori, A. Kawai and K. Obi, *Chem. Phys. Lett.*, 1996, **262**, 125–130.

46 M. Mitsui, K. Takeda, Y. Kobori, A. Kawai and K. Obi, *J. Phys. Chem. A*, 2004, **108**, 1120–1126.

47 A. Kawai, T. Okutsu and K. Obi, *J. Phys. Chem.*, 1991, **95**, 9130–9134.

48 M. De Nardi, S. Antonello, D. Jiang, F. Pan, K. Rissanen, M. Ruzzi, A. Venzo, A. Zoleo and F. Maran, *ACS Nano*, 2014, **8**, 8505–8512.

49 M. Agrachev, S. Antonello, T. Dainese, J. A. Gascón, F. Pan, K. Rissanen, M. Ruzzi, A. Venzo, A. Zoleo and F. Maran, *Chem. Sci.*, 2016, **7**, 6910–6918.

50 S. Antonello, T. Dainese, F. Pan, K. Rissanen and F. Maran, *J. Am. Chem. Soc.*, 2017, **139**, 4168–4174.

51 A. Venzo, S. Antonello, J. A. Gascón, I. Guryanov, R. D. Leapman, N. V. Perera, A. Sousa, M. Zamuner, A. Zanella and F. Maran, *Anal. Chem.*, 2011, **83**, 6355–6362.

52 S. Antonello, M. Hesari, F. Polo and F. Maran, *Nanoscale*, 2012, **4**, 5333–5342.

53 I. Rosenthal, Chemical and Physical Sources of Singlet Oxygen, in *Singlet O$_2$*, ed. A. A. Frimer, CRC Press, Boca Raton, 1985, vol. I, pp. 13–38.

54 A. Kawai and K. Shibuya, *J. Photochem. Photobiol., C*, 2006, **7**, 89–103.

55 M. J. Povich, *J. Phys. Chem.*, 1975, **79**, 1106–1109.

56 M. Bregnhøj, M. Westberg, F. Jensen and P. R. Ogilby, *Phys. Chem. Chem. Phys.*, 2016, **18**, 22946–22961.

57 A. A. Gorman, I. Hamblett, C. Lambert, B. Spencer and M. C. Standen, *J. Am. Chem. Soc.*, 1988, **110**, 8053–8059.

58 J. Zhang, C. Jiang, J. P. Figueiró Longo, R. B. Azevedo, H. Zhang and L. A. Muehlmann, *Acta Pharm. Sin. B*, 2018, **8**, 137–146.

59 C. Tanielian and C. Wolff, *Photochem. Photobiol.*, 1988, **48**, 277–280.

60 S. M. Bachilo and R. B. Weisman, *J. Phys. Chem. A*, 2000, **104**, 7711–7714.

61 C. Tanielian and C. Wolff, *J. Phys. Chem.*, 1995, **99**, 9825–9830.

62 M. Pineiro, A. L. Carvalho, M. M. Pereira, A. M. d'A. Rocha Gonsalves, L. G. Arnaut and S. J. Formosinho, *Chem.–Eur. J.*, 1998, **4**, 2299–2307.

63 C. Ouannès and T. Wilson, *J. Am. Chem. Soc.*, 1968, **90**, 6527–6528.

64 C. Schweitzer, Z. Mehrdad, F. Shafii and R. Schmidt, *Phys. Chem. Chem. Phys.*, 2001, **3**, 3095–3101.

65 E. A. Ogryzlo and C. W. Tang, *J. Am. Chem. Soc.*, 1970, **92**, 5034–5036.

66 A. P. Darmanyan, W. S. Jenks and P. Jardon, *J. Phys. Chem. A*, 1998, **102**, 7420–7426.

67 C. Schweitzer, Z. Mehrdad, F. Shafii and R. Schmidt, *J. Phys. Chem. A*, 2001, **105**, 5310–5316.

68 B. F. Minaev, *Theor. Exp. Chem.*, 1984, **20**, 199–201.

69 S. Antonello, G. Arrigoni, T. Dainese, M. De Nardi, G. Parisio, L. Perotti, A. René, A. Venzo and F. Maran, *ACS Nano*, 2014, **8**, 2788–2795.

70 S. Antonello, T. Dainese, M. De Nardi, L. Perotti and F. Maran, *ChemElectroChem*, 2016, **3**, 1237–1244.

71 S. Antonello, A. H. Holm, E. Instuli and F. Maran, *J. Am. Chem. Soc.*, 2007, **129**, 9836–9837.

72 S. Wang, Y. Song, S. Jin, X. Liu, J. Zhang, Y. Pei, X. Meng, M. Chen, P. Li and M. Zhu, *J. Am. Chem. Soc.*, 2015, **137**, 4018–4021.

73 C. Yao, Y.-j. Lin, J. Yuan, L. Liao, M. Zhu, L.-h. Weng, J. Yang and Z. Wu, *J. Am. Chem. Soc.*, 2015, **137**, 15350–15353.

74 L. Liao, S. Zhou, Y. Dai, L. Liu, C. Yao, C. Fu, J. Yang and Z. Wu, *J. Am. Chem. Soc.*, 2015, **137**, 9511–9514.

75 M. Zhou, C. Yao, M. Y. Sfeir, T. Higaki, Z. Wu and R. Jin, *J. Phys. Chem. C*, 2018, **122**, 13435–13442.

76 X. Wen, P. Yu, Y. R. Toh, A. C. Hsu, Y. C. Lee and J. Tang, *J. Phys. Chem. C*, 2012, **116**, 19032–19038.

77 R. Castro-Olivares, G. Günter, A. L. Zanocco and E. Lemp, *J. Photochem. Photobiol., A*, 2009, **207**, 160–166.

78 I. B. Berlman, *Handbook of Fluorescence Spectra of Aromatic Molecules*, Academic Press, New York, 1971.

79 J. P. Dinnocenzo, P. B. Merkel and S. Farid, *J. Phys. Chem. A*, 2017, **121**, 7903–7909.

80 A. P. Woodham, G. Meijer and A. Fielicke, *Angew. Chem., Int. Ed.*, 2012, **51**, 4444–4447.

81 A. P. Woodham, G. Meijer and A. Fielicke, *J. Am. Chem. Soc.*, 2013, **135**, 1727–1730.

82 S. Bhat, R. P. Narayanan, A. Baksi, P. Chakraborty, G. Paramasivam, R. R. J. Methikkalam and A. Nag, *J. Phys. Chem. C*, 2018, **122**, 19455–19462.

83 L. D. Zusman, *Chem. Phys.*, 1980, **49**, 295–304.

84 N. Sutin, *Prog. Inorg. Chem.*, 1983, **30**, 441–498.

85 R. A. Marcus and N. Sutin, *Biochim. Biophys. Acta*, 1985, **811**, 265–322.

86 A. B. Meneses, S. Antonello, M.-C. Arévalo, C. C. González, J. Sharma, A. N. Wallette, M. S. Workentin and F. Maran, *Chem.–Eur. J.*, 2007, **13**, 7983–7995.

87 S. Antonello, N. V. Perera, M. Ruzzi, J. A. Gascón and F. Maran, *J. Am. Chem. Soc.*, 2013, **135**, 15585–15594.

88 A. Ignaczak, W. Schmickler and S. Bartenschlager, *J. Electroanal. Chem.*, 2006, **586**, 297–307.

89 D. Rehm and A. Weller, *Isr. J. Chem.*, 1970, **8**, 259–271.

90 IUPAC, *Compendium of Chemical Terminology*, compiled by A. D. McNaught and A. Wilkinson, Blackwell Scientific Publications, Oxford, 2nd edn (the "Gold Book"), 1997, online version (2019) created by S. J. Chalk, ISBN 0-9678550-9-8, DOI: 10.1351/goldbook.

91 C. Schweitzer, Z. Mehrdad, F. Shafii and R. Schmidt, *Phys. Chem. Chem. Phys.*, 2001, **3**, 3095–3101.

92 S. Fukuzumi, S. Fujita, T. Suenobu, H. Yamada, H. Imahori, Y. Araki and O. Ito, *J. Phys. Chem. A*, 2002, **106**, 1241–1247.

93 B. F. Minaev, *Russ. Chem. Rev.*, 2007, **76**, 988–1010.

94 S. Farid, J. P. Dinnocenzo, P. B. Merkel, R. H. Young and D. Shukla, *J. Am. Chem. Soc.*, 2011, **133**, 4791–4801.

95 O. J. H. Chai, Z. Liu, T. Chen and J. Xie, *Nanoscale*, 2019, **11**, 20437–20448.

96 T. Kawawaki, Y. Negishi and H. Kawasaki, *Nanoscale Adv.*, 2020, **2**, 17–36.

97 A. B. Meneses, S. Antonello, M.-C. Arévalo and F. Maran, *Electroanal*, 2006, **18**, 363–370.